Interface Behavior

CrossMark

The role of carbon and tungsten disulphide nanotubes in the fracture of polymer-interlayered ceramic composites: a microscopy study

Konstantin Livanov[1], Hans Jelitto[2], Gerold A. Schneider[2], and H. Daniel Wagner[1,*]

[1] Department of Materials and Interfaces, Weizmann Institute of Science, 76100 Rehovot, Israel
[2] Institute of Advanced Ceramics, Hamburg University of Technology, 21073 Hamburg, Germany

ABSTRACT

Multi-walled carbon nanotubes (MWNT) and tungsten disulphide nanotubes (WS$_2$-INT) have been widely used to improve the strength and toughness of composite materials. The mechanisms of such improvements are extensively studied, but it is not often clear what prompts a specific reinforcement mechanism to work. In this work we prepared two similar systems reinforced with different nanofillers (MWNT and WS$_2$-INT). Using in situ optical microscopy and post-fracture electron microscopy, we established that using different nanofillers results in a different type of fracture and a different reinforcement mechanism. When compared to non-reinforced composites both systems showed significant improvements in both strength and fracture toughness.

Introduction

Nanoscale fillers, such as carbon nanotubes or tungsten disulphide nanotubes, have been extensively used to affect the mechanical properties of composite materials [1–4]. Being exceptionally strong and stiff themselves [5–7], traditionally, they are incorporated in polymer [8–11] or ceramic matrices [12, 13] to improve the matrix' stiffness, strength, fracture toughness or combination of these properties. The effect is varied, spanning from several [14] to hundreds of percentage [15, 16] increases, and heavily depends on the filler geometry [17], matrix properties [9, 18] and the incorporation method [19, 20].

The ways these improvements occur also vary. Various reinforcing mechanisms, both intrinsic and extrinsic, are reported in the literature: nanotube pull-out [21], crack bridging [22], grain bridging [23], layer delamination, crack deflection/bifurcation [24–29] and interphase reinforcement [19] are just a few of them. Most either dissipate the fracture energy, or inhibit crack propagation, thereby delaying the catastrophic failure of the structure.

Not all mechanisms simultaneously occur in a given composite. They are strongly dependent on the nanofiller used and the way it is incorporated in the structure. Parameters, such as dispersion quality, degree of ordering of the nanofillers and their

Address correspondence to E-mail: daniel.wagner@weizmann.ac.il

Springer

concentration, as well as the shape of the fillers [17], their orientation [29] and their chemical composition (which affects both the mechanical properties of the fillers and their adhesion to the composite matrix [30, 31]), play a crucial role in the reinforcement mechanism that is activated [23, 32].

In this work we propose to study the mechanical properties and fracture behaviour of layered ceramic–polymer composites reinforced with either multi-walled carbon nanotubes (MWNT) or tungsten disulphide nanotubes (WS$_2$-INT). The composites are prepared by "evaporation-driven self-assembly of polymers" (EDSAP) [19, 33]. This process allows creating a thin (2, 3 µm) uniform nanocomposite coating on a flat substrate. The coating consists of a polymer (in this case, polyvinyl butyral, PVB) and nanoscale filler, namely either MWNT or WS$_2$-INT. A schematic illustration of the EDSAP process is shown in Fig. 1. A fuller description of the EDSAP method and its physical origins can be found in the Supplementary material for this work or in our previous studies [19, 33]. The coated substrates are then hotpressed together to make two-layer structures (Fig. 2a). The strength (σ_c) and the apparent work of fracture (W_f) of these composites are tested in a threepoint bending configuration. In situ optical microscopy observation and post-fracture electron microscopy observations are then used to identify the reinforcing mechanism operating in each case.

Materials and methods

Composite preparation

PVB–MWNT films

The organic films were prepared by an EDSAP approach developed in our previous work [19, 33]. The substrates were either alumina or microscope cover glass. In a typical procedure CVD-grown MWNTs (50 mg, 0.5 mg/ml, typical dimensions: length: 3–10 µm, diameter: 8–10 nm) were put into 100 ml of Tetrahydrofuran (THF) and sonicated for 20 min. Then, 1 ml of Tryton-X surfactant (1 wt%) and 0.5 gr of PVB (0.5 wt%) were added to the dispersion, which was sonicated for an additional 2 h [34]. The resulting dispersion remains stable for several weeks in ambient conditions. 0.25-mm-thick Al$_2$O$_3$ plates (99.6% pure, as-fired, unpolished, purchased from Valley Design Corp., Shirley, MA) were cut using a diamond saw into 30 mm × 3.5 mm substrate slides. Microscope cover glass (1 mm thick) was used as is. The slides and cover glasses were sonicated in DI water, ethanol and acetone and then put in a vertical position into a specially designed EDSAP tank. PVB–MWNT dispersion was filtered through cotton wool to remove large aggregates, and then added to the tank until the substrates were completely covered by the liquid. The tanks were left in ambient conditions for 20 h until all the solvent evaporated (Fig. 1). The substrates were then carefully rinsed with water and dried in air. The average thickness of the coating was measured to be 2.5 ± 0.5 µm, and the volume fraction of MWNT in
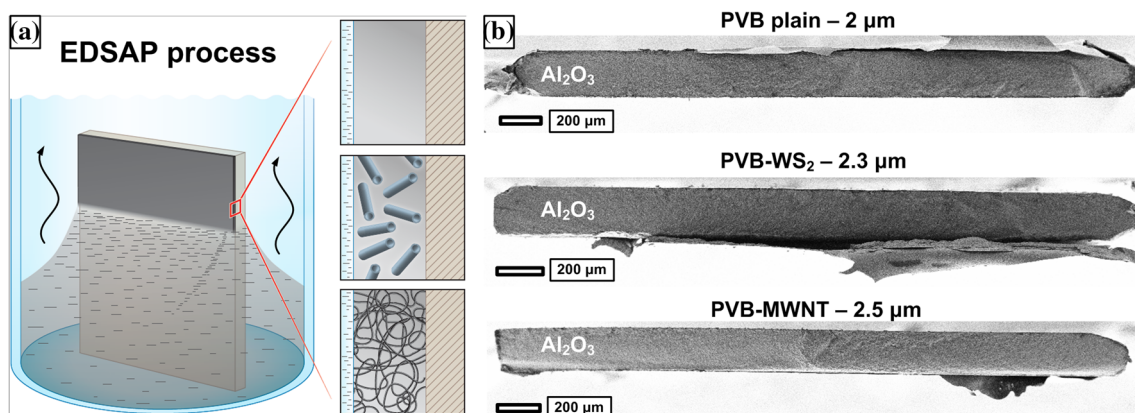
Figure 1 EDSAP process. **a** Schematic representation of EDSAP process. The insets correspond to plain PVB (top), PVB–WS$_2$ (middle) and PVB–MWNT (bottom) composites. **b** The resulting films with their respective thicknesses.
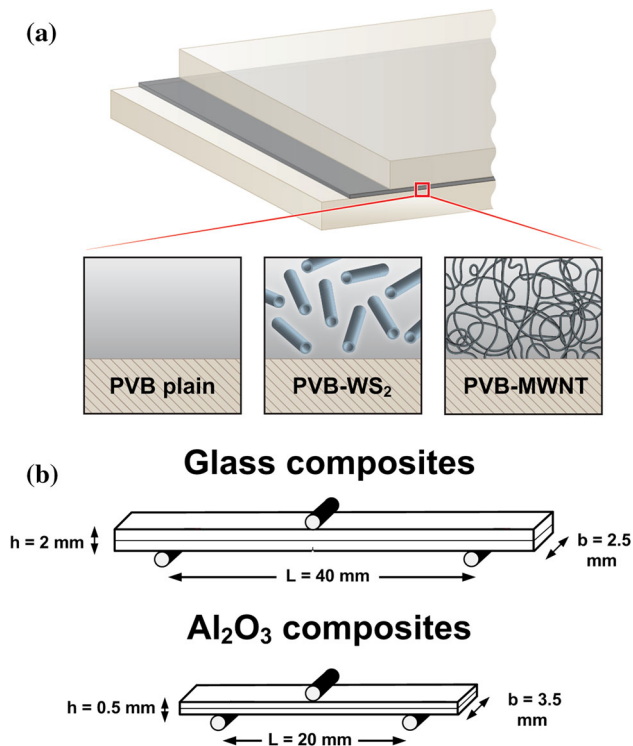
Figure 2 Layered composites. **a** Schematic representation of a two-layered composite. The insets correspond to plain PVB (left), PVB–WS$_2$ (middle) and PVB–MWNT (right) composites. **b** Schematic representations of the measurement process of glass (top) and Al$_2$O$_3$ (bottom) composites.

the PVB film was measured to be $7 \pm 2\%$, according to our previous work [33].

PVB–WS$_2$ films

The same general procedure was used for WS$_2$-INT films. 500 mg of WS$_2$-INT (5 mg/ml, typical dimensions: length: 2–7 µm, diameter: 30–150 nm) powder were put into 100 ml of ethanol and sonicated for 20 min. Then, 1 ml of Tryton-X surfactant (1 wt%) and 1 gr of PVB (1 wt%) were added to the dispersion, which was sonicated for an additional 2 h [34]. Resulting dispersion was stable in ambient conditions for several days, and then its colour changed from dark brown to light brown due to WS$_2$ nanotubes oxidation. All further experiments were done prior to that point. 30 mm × 3.5 mm × 0.25 mm Al$_2$O$_3$ substrates and microscope cover glasses were sonicated in DI water, ethanol and acetone and then put in a vertical position into a specially designed EDSAP tank. PVB–WS$_2$ dispersion was then added to the tank until the substrates were completely covered

by the liquid. The tanks were left in ambient conditions for 30 h until all the solvent evaporated (Fig. 1). The substrates were then carefully rinsed with water and dried in air. The average thickness of the coating was measured to be 2.3 ± 0.9 µm, and the volume fraction of MWNT in the PVB film was measured to be $11 \pm 2\%$, according to our previous work [33].

Plain PVB films (control)

Non-reinforced PVB films were prepared for control purposes to measure the influence of nanofillers. For that, 1 ml of Tryton-X surfactant and 1 gr of PVB were added to 100 ml of THF, which was sonicated for 2 h. 30 mm × 3.5 mm × 0.25 mm Al$_2$O$_3$ substrates and microscope cover glasses were sonicated in DI water, ethanol and acetone and then put in a vertical position into a specially designed EDSAP tank. PVB solution was then added to the tank until the substrates were completely covered by the liquid. The tanks were left in ambient conditions for 20 h until all the solvent evaporated (Fig. 1). The substrates were then carefully rinsed with water and dried in air. The average thickness of the coating was measured to be 2.0 ± 0.7 µm, according to our previous work [33].

Multi-layer composite preparation

Multi-layered structures were prepared from the coated specimens [24]. Two- and four-layered structures were prepared from Al$_2$O$_3$ substrates, and only two-layered structures were made from the thicker microscope glass substrates. All the multi-layered structures were prepared using the same procedure. Two (or four)-coated substrates were tightly held together and then put into a hot-press under 15 kg at 150 °C for 20 min. The thickness change after the hot pressing was negligible compared to the total thickness of the multi-layers. About 60–70% of the structures prepared in this manner were not visibly fractured and were used as is in mechanical measurements. The temperature was lowered gradually and slowly in order to relieve the specimens from residual stress. The microscope glass slides were cut using a diamond saw to final dimensions of 50 mm × 2.5 mm × 2 mm. The glass multi-layers were notched first using the same diamond saw and then a razor blade in a home-made apparatus, to the total depth of 0.3–0.5 mm, representing 15–25% of the

whole structure's height, to achieve stable crack growth. The alumina multi-layers remained unnotched due to their dimensions and notching instrumentation restrictions. The resulting two-layered composites are schematically shown in Fig. 2.

Bending tests

Critical strength at fracture (σ_c) and apparent work of fracture (W_f) of the multi-layered structures were measured in three-point bending configuration with a custom-made stiff testing machine (developed at TUHH, Institute of Advanced Ceramics) [35–37]. The machine used an automated computer control of stable crack growth and was equipped with a quartz dynamic load cell type 9212 (Kistler) (high sensitivity of 11.3 pC/N) and a position sensor 1-WI/2MM-T (HBM). The loading spans for Al_2O_3 and glass specimens were 20 and 40 mm, respectively, and the crosshead speed was 0.2 µm/s (see Fig. 2b for a schematic description of the experiment).

The mechanical testing device allowed a precise control of the displacement. Fast partial unloading of the sample was possible, to enable finer control of the crack growth. Since the material is not homogenous and, as will be shown, the crack path deflects strongly at interfaces, the application of classical fracture mechanical analysis was problematic. Therefore, only the apparent work of fracture (W_f) was calculated as a measure of fracture toughness:

$$W_f = {S_{LD}}/{2b(h - a_0)} \tag{1}$$

where S_{LD} is the total area under the load–deflection curve, b is the specimen width, h is the specimen height and a_0 is the notch depth [24, 38]. These definitions can also be found in Fig. 2b, together with the specimens' dimensions. The term "apparent" is used to emphasize that the transverse cross section ($b \times (h - a_0)$) is used to normalize the energy, rather than the true crack area, which includes the delamination area [33]. The real work of fracture is probably slightly larger than the measured values, because unstable fracture of single layers creates kinetic energy, which is not captured in the load–deflection curves. At least five specimens of each type were tested.

The critical strength (σ_c) of the multi-layered structures was calculated from the three-point bending experiments, as follows:

$$\sigma_c = \frac{3F_{max}L}{2b(h - a_0)^2} \tag{2}$$

where L is the support span in the three-point bending test, b is the specimen width, h is the specimen height, a_0 is the notch depth, and F_{max} is the highest measured load [24, 39, 40].

In situ optical microscope observations

For in situ optical observations of the fracture process, a CCD-Camera JAI CB-140 GE with a Nikon (20×0.35 WD = 20.5 mm) micro-objective, combined with TV-Zoom Optics 70XL $0.3 \times - 2.2 \times$ (Opto, Germany) was used.

Post-fracture SEM observations

High-resolution scanning electron microscope (HR-SEM) images were obtained using SUPRA-55 VP Zeiss and ULTRA-55 Zeiss instruments using an In-Lens detector. Images were collected at an acceleration voltage of 3 kV and working distance of 4, 5 mm. Prior to SEM imaging, the samples were sputtered with gold–palladium alloy using an Edwards S150 sputter coater instrument to prevent sample charging.

Results and discussion

First we describe the typical fracture process of a WS_2-reinforced glass composite (PVB–WS_2). The load–deflection (LD) plot of the process (black line) and optical microscope images taken during the fracture process are shown in Fig. 3. The letters on the LD plot correspond to the respective microscope images. The grey dashed line on the LD plot is typical of a plain (non-reinforced) specimen.

After the initial loading and the first load drop (referred to as "pop-in" [24]), that signifies the failure of the bottom, notched layer, a thin crack is clearly seen on the bottom layer of the composite (white arrow in Fig. 3b). That crack continues to widen (Fig. 3c) until a second pop-in occurs (Fig. 3d). Surprisingly, the structure is not completely failed even after both glass layers are cracked—this behaviour is typical of WS_2-reinforced composites. The two cracks visibly continue to widen (Fig. 3d–f) as the polymer interlayer deforms and eventually fails (Fig. 3g). Note
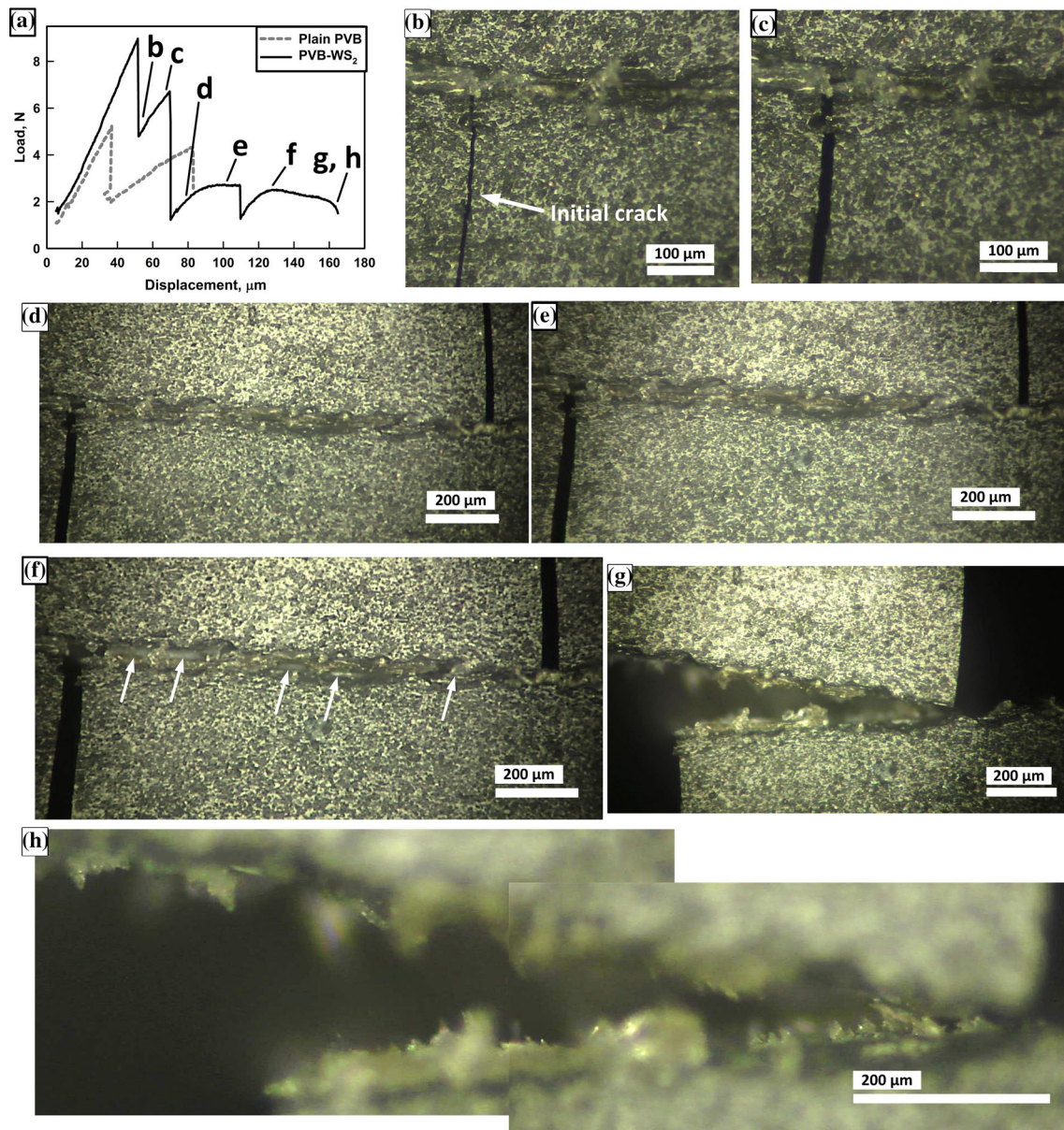
Figure 3 Fracture of PVB–WS₂ composites. **a** Typical LD plot of a PVB–WS₂ (black) and plain PVB (grey) specimens. The letters on the LD plot correspond to the respective microscope images. **b–h** In situ optical micrographs taken during the fracture of the same specimen: initial crack appears after the first "pop-in" (**b**), followed by crack widening (**c**) and a second "pop-in" leading to the second crack (**d**). Both cracks continue to open (**e, f**) until the polymer interlayer fails (**g, h**). Refer to text for a more thorough description of the fracture process.

the cavities that appear in the polymer interlayer after the third pop-in (accentuated by white arrows in Fig. 3f). Figure 3h is a zoom-in of a fracture polymer interlayer, showing multiple deformations that occur during the fracture process.

A typical fracture process of the MWNT-reinforced glass composite (PVB–MWNT) is quite different from the one just described. An LD plot of such process

(black line) and the optical microscope images taken during the fracture process are shown in Fig. 4. The letters on the LD plot correspond to the respective microscope images. The grey dashed line on the LD plot represents a typical LD plot of a plain (non-re-inforced) specimen.

After the first pop-in a crack is visible and begins to widen, just like in the case above (Fig. 4b, c).
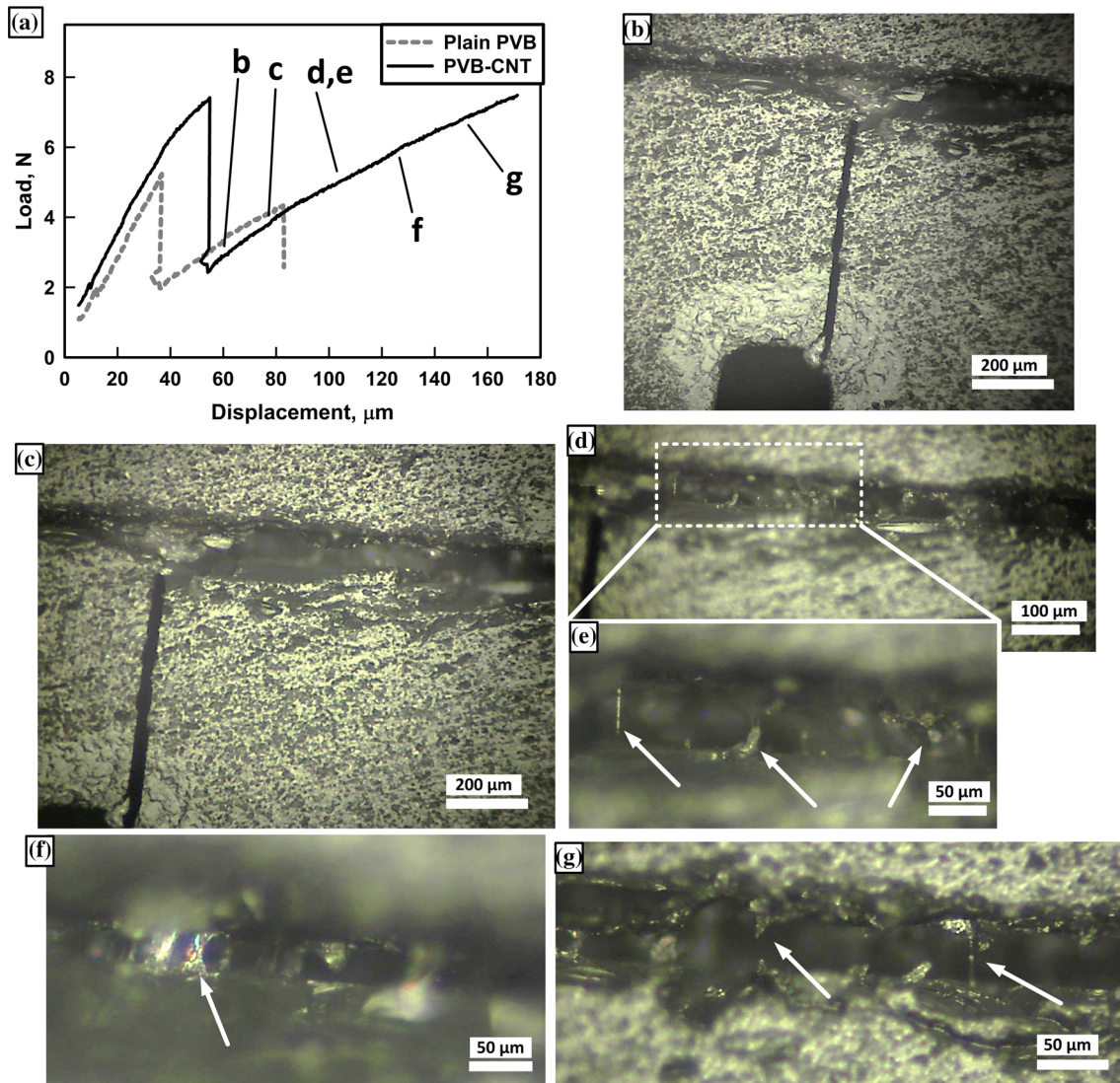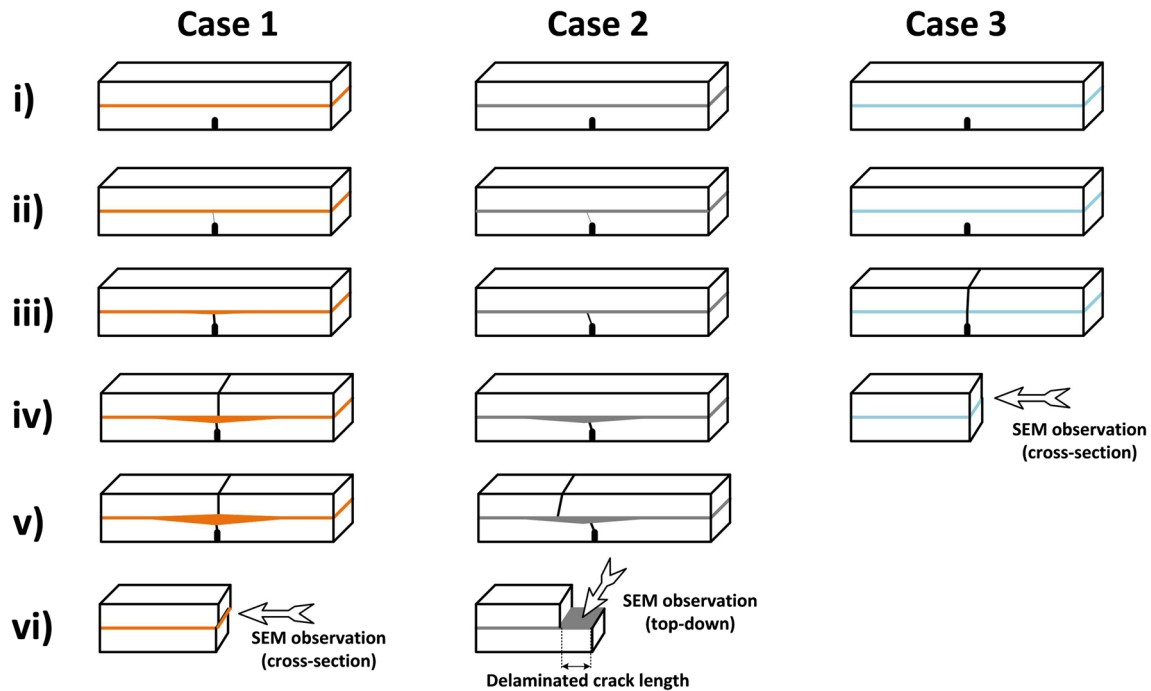
Figure 4 Fracture of PVB–MWNT composites. **a** Typical LD plot of a PVB–MWNT (black) and plain PVB (grey) specimens. **b**–**g** In situ optical micrographs taken during the fracture of the same specimen: initial crack appears and widens after the first "pop-in" (**b**, **c**). A crack bifurcates into the polymer interlayer, and it begins to fail (**d**, **e**). Shear hackles are developed (**f**) and fail (**g**) under tensile forces. Refer to text for a more thorough description of the fracture process.

However, the second pop-in does not appear as soon. Instead, a crack bifurcates, and delamination region begins to develop (Fig. 4d). In the zoom-in image (Fig. 4e) the development of polymer ligaments and shear hackles (pointed to by white arrows)—deformations common in soft matrix composites [41]—can be clearly seen. This behaviour continues, and the shear hackles are subjected to tensile forces (Fig. 4f), which often contributes to higher energies required for crack bifurcation. Eventually they fail under tension (for example, as shown by white arrows in Fig. 4g). After the second pop-in occurs, the composite fails altogether.

The Al$_2$O$_3$ composites show a generally similar behaviour. The LD plots and corresponding optical microscopy images for the Al$_2$O$_3$ composites can be found in the Supplementary material. Figure 5 summarizes the difference between the failure processes of the different composites. The process presented as "Case 1" is typical of the PVB–WS$_2$ specimens: (1) the structure is put under load; (2) a crack in the notched layer appears; (3) the crack widens; (4) a crack appears in the second layer and the interlayer is deformed; (5) the interlayer is further deformed; and (6) the structure fails. The process presented as "Case 2" is typical to the PVB–MWNT specimens: (1) the

Figure 5 Three cases of specimen fracture. Schematic representation of three different cases observed during fracture of two-layered plain PVB, PVB–WS$_2$ and PVB–MWNT composites.

structure is put under load; (2) a crack appears in the second layer; (3) the crack widens; (4) the interlayer is deformed; (5) the interlayer is further deformed; and (6) the structure fails. The process presented as "Case 3" is likely in all three types of specimens (plain PVB, PVB–WS$_2$ and PVB–MWNT) and is more common in Al$_2$O$_3$ structures than in glass structures, and in plain structure than in reinforced ones. During "Case 3" fracture: (1) the structure is put under load; (2) no visible changes occur over a longer period of time compared to the other two cases; (3) cracks in both layers appear, and almost immediately; and (4) the structure fails. Steps (3) and (4) often occur simultaneously and are impossible to capture on camera separately. It can be argued that "Case 3" fracture is just an extreme variant of "Case 1" fracture, in which the polymer interlayer is unable to prevent the crack from propagating into the second ceramic layer. The fact that it is more common in plain, non-reinforced structures corresponds well with the structures' mechanical properties.

An additional important point of distinction between the "Case 1" and "Case 2" fractures is the delamination crack length, schematically demonstrated in Fig. 5, "Case 2" column. The delamination crack length in "Case 2" fracture is typically significantly longer than that in "Case 1" and "Case 3" fractures, 3–5 mm as opposed to 0–2 mm of the latter. This may account for some additional energy dissipated during the fracture process and, as a result, higher work of fracture.

The mechanical properties of glass and Al$_2$O$_3$ composites, including critical strength (σ_c), work of fracture (W_f) and average displacement before fracture, and the type of fracture typical to the structure, are summarized in Tables 1 and 2, respectively. The mechanical results correspond well to the in situ observations: the PVB–WS$_2$ specimens show the highest strength, whereas the PVB–MWNT specimens—the highest work of fracture and displacement. It is easy to notice that the higher strength values correspond to the "Case 1" fractures (Fig. 5), likely due to better stress transfer between the layers; the higher work of fracture values correspond to the "Case 2" fracture, likely due to energy dissipated during the delamination process. High error values in both tables may be attributed to general brittleness of the system or on the effect of residual stresses accumulated during specimen preparation.

Due to the different modes of composite fracture in different cases, the SEM examination of the fractured specimens also was performed differently.

Table 1 Fracture type and mechanical properties of two-layered glass composites

	Fracture	Strength (MPa)	W_f (kJ/m^2)	Displacement (μm)
Plain PVB	Case 1, Case 2 and Case 3	24.6 ± 3.4	0.035 ± 0.014	81 ± 24
PVB–WS$_2$	Mostly Case 1, some Case 3	42.3 ± 8.9	0.069 ± 0.018	119 ± 28
PVB–MWNT	Case 2	37.8 ± 9.3	0.096 ± 0.069	157 ± 59

Table 2 Fracture type and mechanical properties of two-layered Al$_2$O$_3$ composites

	Fracture	Strength (MPa)	W_f (kJ/m^2)	Displacement (μm)
Plain PVB	Mostly Case 3, some Case 1 and Case 2	155 ± 26	0.15 ± 0.05	154 ± 27
PVB–WS$_2$	Mostly Case 1, some Case 3	357 ± 68	0.27 ± 0.07	162 ± 22
PVB–MWNT	Mostly Case 2, some Case 3	303 ± 105	0.32 ± 0.06	219 ± 15

Specifically, after "Case 1" or "Case 3" fracture, the cross section of the fractured specimens was investigated. After "Case 2" fracture, the cross-sectional examination was usually impossible due to the interlayer deformation. Instead, a top-down investigation of the delaminated layer was performed. Figure 5 shows the SEM observation perspective (cross section, top-down) that provides the most data in each fracture case.

Figure 6 shows a cross-sectional view of the WS$_2$-reinforced glass specimen after a "Case 1" fracture. The cross section of the fracture surface reveals a large amount of nanotube pull-out, which contributes to the structures' high fracture resistance (Table 1). Some of the cavities left by nanotube pull-out are shown with yellow arrows. Figure 6b, d is zoom-in images of Fig. 6a, c, respectively. In addition, the fracture surface is significantly deformed and in some cases, local delamination of the polymer interlayer from the ceramic layer can be seen (Fig. 6c, d).[1] It can also be observed that as delamination occurs, the WS$_2$ nanotubes do not inhibit the delamination crack propagation, and even may exhibit some degree of alignment along it (Fig. 6d). Such alignment was not observed in as-prepared specimens [33].

Figure 7 is a top-down view of a delaminated section of a PVB–MWNT glass specimen after a "Case 2" fracture. Top-down view SEM observations of fractured specimens show that the organic layer is significantly deformed and torn. The broken "shear

hackles" (shown with white arrows in Fig. 4g) are visible on SEM images, and are pointed to by white arrows as well (Fig. 7a). As a series of zoom-in images (Fig. 7a–d) reveals, the torn shear hackles show extensive nanotube pull-out (Fig. 7c–e) and in some cases even nanotube bridging (Fig. 7f) of the cracked polymer layer. This hints to a mechanism similar to the interphasial deformation [19]. The cross-sectional observations, as opposed to the "top-down ones", of the "Case 2" fractured specimens do not reveal significant nanotube pull-out during the fracture of the polymer interlayer. SEM images of fractured plain PVB composites are shown in the Supplementary materials.

To clarify this we summarize the difference between "Case 1" and "Case 2" fractures at the nanotube level, based on SEM observations. In "Case 1" fracture, typical of PVB–WS$_2$ specimens, the nanotubes are pulled out primarily during crack propagation *through* the polymer interlayer. In "Case 2" fracture, typical of PVB–MWNT specimens, the nanotubes are pulled out primarily during the crack propagation *along* the polymer interlayer, that is, the process of crack bifurcation and subsequent delamination, during formation and failure of structures known as "shear hackles" [41] (shown with white arrows in Figs. 4g, 7a). This fundamental difference has an effect on the mechanical properties of the two structures.

To further investigate the reinforcement mechanisms in more complex structures we prepared four-layered Al$_2$O$_3$ specimens of all three varieties—with

---

[1] The polymer interlayer in this case is thicker than typical.

Figure 6 Post-fracture SEM observations of PVB–WS$_2$ specimens. **a** A typical cross section of a PVB–WS$_2$ specimen, showing WS$_2$ nanotubes pull-out. **b** Zoom-in of **a**. **c** Local delamination of the polymer interlayer in a PVB–WS$_2$ specimen. **d** Zoom-in of **c**. Yellow arrows point to cavities left after a nanotube pull-out.

SEM observation (cross-section)
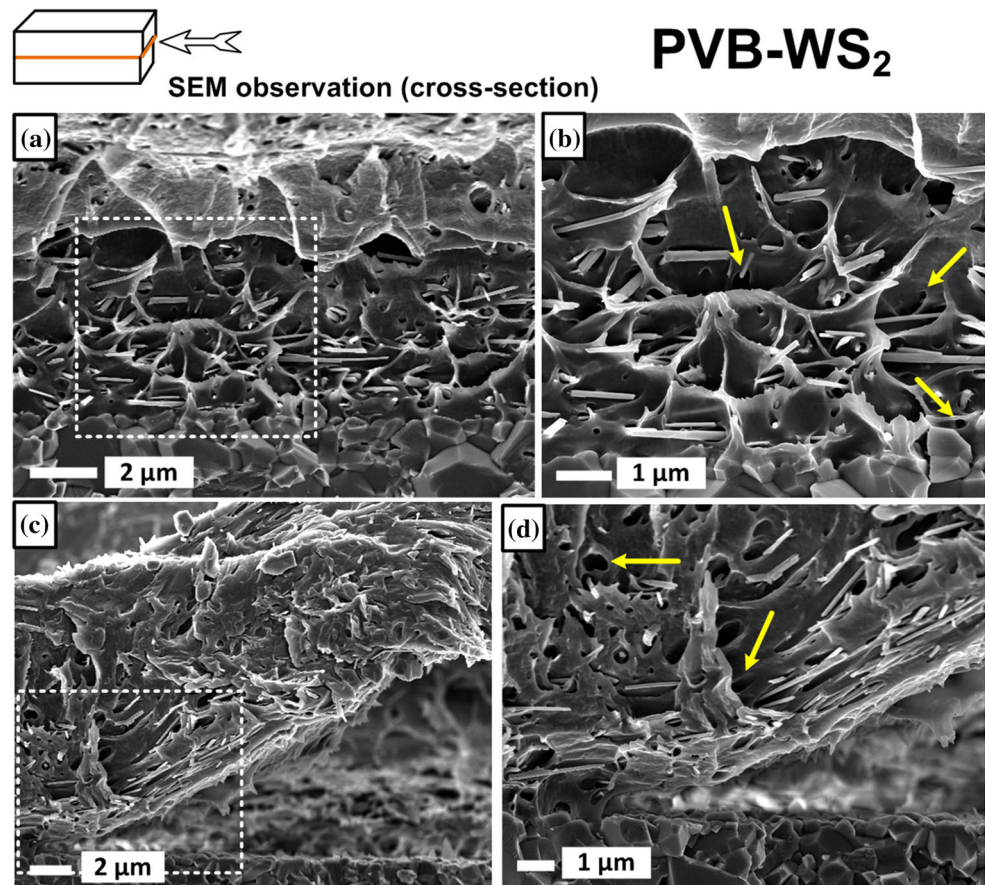
PVB-WS$_2$

plain PVB, PVB–WS$_2$ and PVB–MWNT interlayers. The mechanical measurements for all specimen types are summarized in Table 3. At least five specimens of each type were tested.

Table 3 shows that multi-layered structures are less varied in terms of their mechanical properties than those presented above. The work of fracture of all three types is higher than corresponding values of two-layered structures, in agreement with previous studies [19, 24]. The strength values are higher as well, in some cases reaching and even exceeding the Al$_2$O$_3$ bulk strength values [24, 33, 42]. This indicates a very efficient stress transfer between the ceramic layers [29, 43].

The failure process of all the four-layered structures was also more varied and complex than that of the two-layered ones. Instead of two major pop-ups (failures of two ceramic layers), that can be either close to each other ("Case 1" and "Case 3") or far from each other ("Case 2") in terms of measurement time and distance, with four-layered composites there are now four pop-ins. Each two pop-ins may occur together or separately, which makes the analysis of

the fracture process difficult and unclear. The only observation that can be made in this case is that MWNT-reinforced specimens favour the "Case 2" fracture process. This is further supported by the fact that fractured PVB–MWNT specimens have a longer average delaminated crack length (Fig. 5) compared to any other specimens.

It is important to note the limitations of this study concerning used materials, namely the nanoreinforcements. MWNT and WS$_2$-INT differ not only in their aspect ratios, but in many other parameters as well. A few important ones are their chemical composition, interactions with the PVB matrix and the solvents and surfactants used during the EDSA process, the shape of their ends (circular/broken), which can affect the abovementioned interactions, their resistance to the mechanical damage during the sonication process. The effect of some of those factors can be understood and taken into account; the effect of others can be minimized. For example, the sonication used in this study to disperse the nanoreinforcements was mild (a sonication bath instead of a sonication probe was used) and kept as short as

Figure 7 Post-fracture SEM observations of PVB–MWNT specimens. **a** A top-down image of a large area of delaminated polymer. White arrows point to "shear hackles", as seen on Fig. 4g. **b**–**d** Consecutive zoom-in images of **a**, showing MWNT pull-out. **e** An additional SEM image of MWNT pull-out. **f** An image of a crack in the polymer layer showing MWNT bridging.
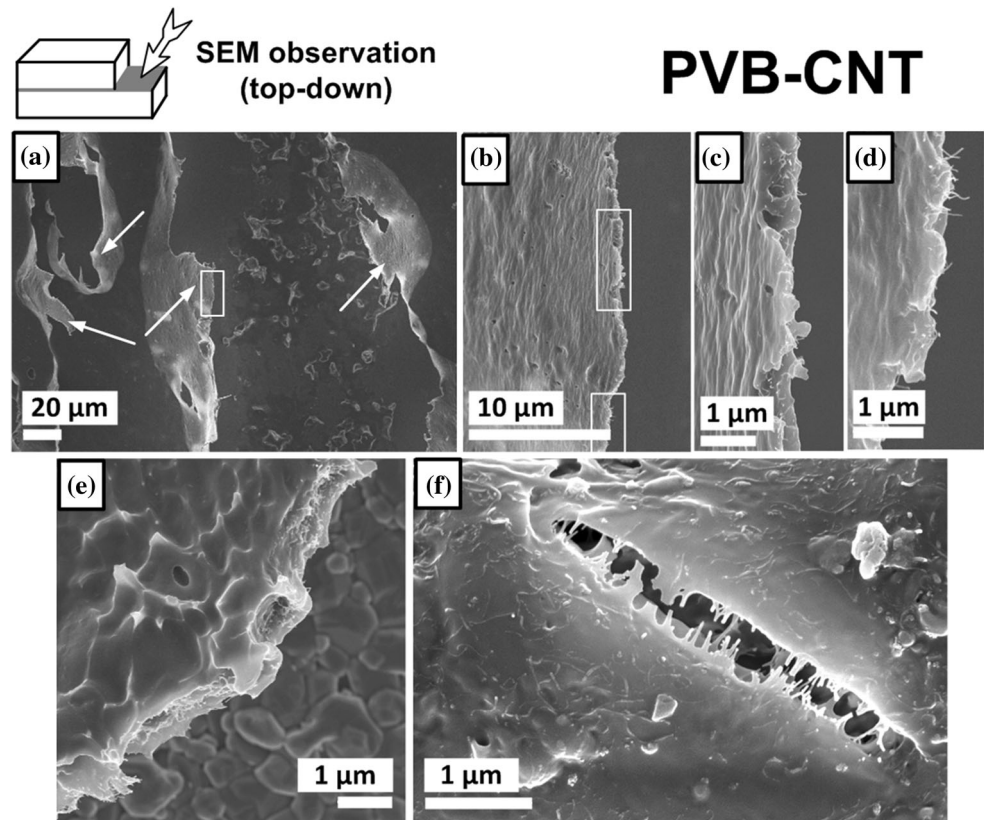
Table 3 Mechanical properties of four-layered Al_2O_3 composites

	Strength (MPa)	W_f (kJ/m^2)	Displacement (μm)
Plain PVB	336 ± 18	0.23 ± 0.02	136 ± 4
PVB–WS$_2$	413 ± 52	0.43 ± 0.05	137 ± 15
PVB–MWNT	367 ± 24	0.46 ± 0.03	164 ± 11

possible. Factors like chemical interactions between the nanotube and the matrix potentially have greater effect on the behaviour of the composite films, such as their yield strength and adhesion to the substrate, and are intrinsic to the system. A deeper understanding of those effects falls out of the scope of current study and may stem from the analytical and computational studies of the system [17, 44, 45].

Conclusions

We investigated the effects of two different nanotubes, tungsten disulphide and multiwall carbon, on the fracture process and mechanical properties of layered ceramic–polymer composites. We have demonstrated that even though the improvements of the composites' strength and work of fracture achieved by the addition of both nanofillers are numerically close to each other, they stem from different fracture mechanisms.

The WS$_2$-INTs are pulled out of the polymer during fracture, thereby strengthening and toughening the polymer interlayer. MWNTs, however, both promote crack bifurcation by reinforcing the interlayer [19] and make resulting layer delamination more costly in terms of energy. They are pulled out from the shear hackles created during the delamination process. The difference between two nanofillers was less pronounced in four-layered structures due to higher variability of the fracture process.

Acknowledgements

Compliance with ethical standards

Conflict of interest   The authors have no conflict of interest to declare.

Electronic supplementary material: The online version of this article (doi:10.1007/s10853-017-1674-5) contains supplementary material, which is available to authorized users.

References

[1] Coleman JN, Khan U, Blau WJ, Gun'ko YK (2006) Small but strong: a review of the mechanical properties of carbon nanotube–polymer composites. Carbon 44:1624–1652

[2] Tenne R, Rosentsveig R, Zak A (2013) Inorganic nanotubes and fullerene-like nanoparticles: synthesis, mechanical properties, and applications. Phys Status Solidi A 210:2253–2258

[3] Naskar AK, Keum JK, Boeman RG (2016) Polymer matrix nanocomposites for automotive structural components. Nat Nanotech 6:1026–1030

[4] Dzenis Y (2008) Structural nanocomposites. Science 314:419–420

[5] Yu M-F, Lourie O, Dyer MJ, Moloni K, Kelly TF, Ruoff RS (2000) Strength and breaking mechanism of multiwalled carbon nanotubes under tensile load. Science 287:637–640

[6] Kaplan-Ashiri I, Tenne R (2016) On the mechanical properties of WS_2 and MoS_2 nanotubes and fullerene-like nanoparticles: in situ electron microscopy measurements. JOM 68:151–167

[7] Barber AH, Kaplan-Ashiri I, Cohen SR, Tenne R, Wagner HD (2005) Stochastic strength of nanotubes: an appraisal of available data. Compos Sci Technol 65:2380–2384

[8] Dufresne A, Paillet M, Putaux JL, Canet R, Carmona F, Delhaes P, Cui S (2002) Processing and characterization of carbon nanotube/poly(styrene- co-butyl acrylate) nanocomposites. J Mater Sci 37:3915–3923. doi:10.1023/A:1019659624567

[9] Gorga RE, Cohen RE (2004) Toughness enhancements in poly(methyl methacrylate) by addition of oriented multiwall carbon nanotubes. J Polym Sci Part B Polym Phys 42:2690–2702

[10] Zhang W, Ge S, Wang Y, Rafailovich MH, Dhez O, Winesett DA, Ade H, Shafi KVPM, Ulman A, Popovitz-Biro R, Tenne R, Sokolov J (2003) Use of functionalized WS_2 nanotubes to produce new polystyrene/polymethylmethacrylate nanocomposites. Polymer 44:2109–2115

[11] Zohar E, Baruch S, Shneider M, Dodiuk H, Kenig S, Tenne R, Wagner HD (2011) The effect of WS_2 nanotubes on the properties of epoxy-based nanocomposites. J Adhesion Sci Technol 25:1603–1617

[12] Zhan GD, Kuntz JD, Wan J, Mukherjee AK (2003) Single-wall carbon nanotubes as attractive toughening agents in alumina-based nanocomposites. Nat Mater 2:38–42

[13] Wang X, Padture NP, Tanaka H (2004) Contact-damage-resistant ceramic/single-wall carbon nanotubes and ceramic/graphite composites. Nat Mater 3:539–544

[14] Mirjalili V, Ramachandramoorthy R, Hubert P (2014) Enhancement of fracture toughness of carbon fiber laminated composites using multi wall carbon nanotubes. Carbon 79:413–423

[15] Veedu VP, Cao A, Li X, Ma K, Soldano C, Kar S, Ajayan PM, Ghasemi-Nejhad MN (2006) Multifunctional composites using reinforced laminae with carbon- nanotube forests. Nat Mater 5:457–462

[16] Mamedov AA, Kotov NA, Prato M, Guldi DM, Wicksted JP, Hirsch A (2002) Molecular design of strong single-wall carbon nanotube/polyelectrolyte multilayer composites. Nat Mater 1:190–194

[17] Greenfeld I, Wagner HD (2015) Nanocomposite toughness, strength and stiffness: role of filler geometry. Nanocomposites 1:3–17

[18] Eitan A, Fisher FT, Andrews R, Brinson LC, Schadler LS (2006) Reinforcement mechanisms in MWCNT-filled polycarbonate. Compos Sci Technol 66:1162–1173

[19] Livanov K, Yang L, Nissenbaum A, Wagner HD (2016) Interphase tuning for stronger and tougher composites. Sci Rep 6:26305

[20] Alhazov D, Zussman E (2012) Study of the energy absorption capabilities of laminated glass using carbon nanotubes. Compos Sci Technol 72:681–687

[21] Evans AG (1990) Perspective on the development of high-toughness ceramics. J Am Ceram Soc 73:187–206

[22] Bouville F, Maire E, Meille S, Van de Moortèle B, Stevenson AJ, Deville S (2014) Strong, tough and stiff bioinspired ceramics from brittle constituents. Nat Mater 13:508–514

[23] Launey ME, Ritchie RO (2009) On the fracture toughness of advanced materials. Adv Mater 21:2103–2110

[24] Livanov K, Jelitto H, Bar-On B, Schulte K, Schneider GA, Wagner DH (2015) Tough alumina/polymer layered composites with high ceramic content. J Am Ceram Soc 98:1285–1291

[25] Mirkhalaf M, Dastjerdi AK, Barthelat F (2014) Overcoming the brittleness of glass through bio-inspiration and micro-architecture. Nat Commun 5:3166

[26] Behr S, Köllner A, Schneider GA (2016) Tailoring toughness and mechanical reliability by controlled defects: nature-inspired composite laminates of laser-perforated yttria-stabilized zirconia. Adv Eng Mater 18(11):1877–1883

[27] Behr S, Jungblut L, Swain MV, Schneider GA (2016) Shear strength and interfacial toughness characterization of sapphire-epoxy interfaces for nacre-inspired composites. ACS Appl Mater Interfaces 8(40):27322–27331

[28] Ritchie RO (2011) The conflicts between strength and toughness. Nat Mater 10:817–822

[29] Norman DA, Robertson RE (2003) The effect of fiber orientation on the toughening of short fiber-reinforced polymers. J Appl Polym Sci 90:2740–2751

[30] Drzal LT, Rich MJ, Lloyd PF (1983) Adhesion of graphite fibers to epoxy matrices: I. The role of fiber surface treatment. J Adhesion 16:1–30

[31] Leger L, Creton C (2008) Adhesion mechanisms at soft polymer interfaces. Phil Trans R Soc A 366:1425–1442

[32] Kim JK, Ma YW (1998) Engineered interfaces in fiber reinforced composite. 1st edn, Chapter 6. Elsevier, New York, pp 239–277

[33] Livanov K, Nissenbaum A, Wagner HD (2016) Nanocomposite thin film coatings for brittle materials. Nanocomposites 2:162–168

[34] Vaisman L, Wagner HD, Marom G (2006) The role of surfactants in dispersion of carbon nanotubes. Adv Colloid Interface Sci 128–130:37–46

[35] Kuebler J, Blugan G, Jelitto H, Schneider GA, Dobedoe R (2007) Structural micro-layered ceramics with surfaces under tension and compression with increasing apparent fracture toughness. Key Eng Mater 336–338:2564–2568

[36] Jelitto H, Hackbarth F, Özcoban H, Schneider GA (2013) Automated control of stable crack growth for r-curve measurements in brittle materials. Exp Mech 53:163–170

[37] Jelitto H, Felten F, Swain MV, Balke H, Schneider GA (2007) Measurement of the total energy release rate for cracks in PZT under combined mechanical and electrical loading. J Appl Mech 74:1197–1211

[38] Krause RF Jr (1988) Rising fracture toughness from the bending strength of indented alumina beams. J Am Ceram Soc 71:338–343

[39] Tattersall HG, Tappin G (1966) The work of fracture and its measurement in metals, ceramics and other materials. J Mater Sci 1:296–301. doi:10.1007/BF00550177

[40] dos Santos SF, Rodrigues JA (2003) Correlation between fracture toughness, work of fracture and fractal dimensions of alumina-mullite-zirconia composites. Mater Res 6:219–222

[41] Piggott M (2002) Load bearing fibre composites, 2nd edn, Chapter 6, Kluwer, p 196

[42] Belenky A, Rittel D (2012) Static and dynamic flexural strength of 99.5% alumina: relation to porosity. Mech Mater 48:43–55

[43] Asloun EM, Nardin M, Schultz J (1989) Stress transfer in single-fibre composites: effect of adhesion, elastic modulus of fibre and matrix, and polymer chain mobility. J Mater Sci 24:1835–1844. doi:10.1007/BF01105713

[44] Yang L, He X, Mei L, Tong L, Wanga R, Li Y (2012) Interfacial shear behavior of 3D composites reinforced with CNT-grafted carbon fibers. Compos A 43:1410–1418

[45] Yang L, Greenfeld I, Wagner HD (2016) Toughness of carbon nanotubes conforms to classic fracture mechanics. Sci Adv 2:e1500969